

RESEARCH ARTICLE

10.1002/2014JE004764

Key Points:

- We investigated the structure of maskelynite from the Lomar crater
- Maskelynite is distinct from both crystalline plagioclase and fused glass
- We show evidence of X-ray and IR anisotropy

Correspondence to:

S. J. Jaret,
Steven.jaret@stonybrook.edu

Citation:

Jaret, S. J., W. R. Woerner, B. L. Phillips, L. Ehm, H. Nekvasil, S. P. Wright, and T. D. Glotch (2015), Maskelynite formation via solid-state transformation: Evidence of infrared and X-ray anisotropy, *J. Geophys. Res. Planets*, 120, 570–587, doi:10.1002/2014JE004764.

Received 24 NOV 2014

Accepted 9 FEB 2015

Accepted article online 11 FEB 2015

Published online 24 MAR 2015

Maskelynite formation via solid-state transformation: Evidence of infrared and X-ray anisotropy

Steven J. Jaret¹, William R. Woerner¹, Brian L. Phillips¹, Lars Ehm^{2,3}, Hanna Nekvasil¹, Shawn P. Wright^{4,5}, and Timothy D. Glotch¹

¹Department of Geosciences, State University of New York at Stony Brook, Stony Brook, New York, USA, ²Mineral Physics Institute, State University of New York at Stony Brook, Stony Brook, New York, USA, ³Photon Sciences Directorate, Brookhaven National Laboratory, Upton, New York, USA, ⁴Department of Geosciences, Auburn University, Auburn, Alabama, USA, ⁵Planetary Science Institute, Tucson, Arizona, USA

Abstract We present the results of a combined study of shocked labradorite from the Lomar crater, India, using optical microscopy, micro-Raman spectroscopy, nuclear magnetic resonance (NMR) spectroscopy, high-energy X-ray total scattering experiments, and micro-Fourier transform infrared (micro-FTIR) spectroscopy. We show that maskelynite of shock class 2 is structurally more similar to fused glass than to crystalline plagioclase. However, there are slight but significant differences—preservation of original preimpact igneous zoning, anisotropy at infrared wavelengths, X-ray anisotropy, and preservation of some intermediate range order—which are all consistent with a solid-state transformation from plagioclase to maskelynite.

1. Introduction

Across the Solar System, impact cratering has played a major role in modifying the surfaces of planetary bodies. On Earth, impact events are important for the evolution of the surface (e.g., the Chicxulub event at the end of the Cretaceous), but impacts are often obscured by other subsequent more active geologic processes, such as plate tectonics, erosion, and deposition. For other planetary bodies such as Mars and the Moon, the lack of major crustal recycling processes allows for greater preservation of the impact cratering record, yielding large expanses of heavily cratered terrain. This terrain is frequently the target of robotic missions because of the potential for exposure of deep crustal lithologies. The Opportunity rover has already encountered material interpreted to be impact ejecta on Mars in Meridiani Planum (e.g., Bounce Rock). The minerals in such material, however, may have been affected by shock. In fact, many of the Martian meteorites, particularly the shergottites, show evidence of moderate to high shock [Stöffler *et al.*, 1991]. Correctly interpreting the geologic histories of heavily cratered planetary bodies requires a full understanding of the crystallographic and structural changes of major minerals induced by shock. To address this issue, we investigated the structural differences between plagioclase and maskelynite of plagioclase composition because plagioclase is a major component of Martian and lunar crustal rocks. In this paper, we first review nomenclature, previous analyses, and interpretations regarding maskelynite. Then, we describe the structure of the maskelynite from the Lomar crater and compare it to that of crystalline plagioclase and fused plagioclase composition glass. Lastly, we discuss possible formation mechanisms and conditions.

2. Background

2.1. Shock Metamorphism

A hypervelocity impact event results in the generation of a shock wave traveling through both the target and the impactor. As a result, the impactor is largely obliterated through melting and/or vaporization and the target rocks undergo a progression of deformation effects [French and Short, 1968; Stöffler, 1971; Melosh, 1989; Osinski and Pierazzo, 2013, and references therein]. Collectively referred to as impact metamorphism, these effects include brecciation, large-scale mechanical mixing of target components, structurally controlled planar deformation features (PDFs), solid-state mineral transformations, formation of high-pressure mineral polymorphs, melting, geochemical mixing of target components, and vaporization of the target and/or impactor [Chao, 1968; von Engelhardt and Stöffler, 1968; French and Koeberl, 2010; Osinski and Pierazzo, 2013, and references within]. A subset of these effects—solid-state internal chemical and structural changes linked directly to the shock wave, i.e., “shock metamorphism”—has received special attention as they are unique

to shock and cannot be produced by nonimpact processes [Alexopoulos *et al.*, 1988; Langenhorst, 2002; Ferrière and Osinski, 2013].

On Earth, the majority of studies of shock metamorphism have focused on the mineralogic changes in tectosilicates, specifically quartz and feldspar, which are known to have crystal structures more susceptible to shock deformation than other silicate types [Stöffler *et al.*, 1991; Johnson *et al.*, 2002; Langenhorst, 2002].

For extraterrestrial materials, shock effects in plagioclase are most relevant for studies of basaltic or anorthositic surfaces, which commonly occur on Mars and the Moon. Shock effects in plagioclase, while less commonly studied than shock effects in quartz, have been well documented from both natural and experimental impacts [Chao, 1968; von Engelhardt and Stöffler, 1968; Stöffler, 1971, 1972; Hörz and Quaide, 1973; Reimold, 1982; Ostertag, 1983; Heymann and Hörz, 1990; Johnson *et al.*, 2002, 2003; Fritz *et al.*, 2005; Johnson, 2012; Jaret *et al.*, 2014; Pickersgill, 2014]. Shock effects in plagioclase represent a progression of deformation and show continued degradation of the crystalline order with increasing shock pressure [Stöffler, 1971; Kieffer *et al.*, 1976; Hanss *et al.*, 1978; Ostertag, 1983; Heymann and Hörz, 1990; Stöffler *et al.*, 1991; Fritz *et al.*, 2005, Johnson, 2012].

Unfortunately, shock classification and barometry calibration is complicated by multiple classification schemes [Short, 1969; Chao, 1968; Stöffler, 1971; Kieffer *et al.*, 1976; Singleton *et al.*, 2011]. In this paper, we follow the classification scheme of Kieffer *et al.* [1976] because it was developed using shocked Lunar basalts.

Regardless of the specific classification scheme used, feldspars generally behave similarly during shock. A major change in plagioclase crystal structure occurs at shock pressures of ~28–34 GPa, at which point plagioclase transforms to a diaplectic glass, often referred to as maskelynite [Bunch *et al.*, 1967; Ostertag, 1983]. Interestingly, the transition to maskelynite is gradational and highly variable depending on specific preshock rock properties (e.g., composition, grain size, porosity, etc) and in some cases plagioclase can retain partial crystallinity up to ~45 GPa [Ostertag, 1983]. Specific feldspar composition directly affects the pressures at which the transition to maskelynite occurs, where more calcic feldspars transform at slightly lower pressure than the more sodic end-members [Ostertag, 1983; Williams and Jeanloz, 1988; Johnson *et al.*, 2002, 2003].

This loss of crystallinity in plagioclase marks a major transition resolvable optically and spectroscopically. Thus, the plagioclase-maskelynite transformation has been the focus of intense research for over 50 years [Milton and De Carli, 1963; Bunch *et al.*, 1967; Stöffler, 1971; Hörz and Quaide, 1973; Bischoff and Stöffler, 1984; Ostertag, 1983; El Goresy *et al.*, 1997; Chen and El Goresy, 2000; Fritz *et al.*, 2005; El Goresy *et al.*, 2013].

2.2. Maskelynite Formation

Despite multiple studies of maskelynite, there remains considerable debate over its formation mechanism. Much of the debate centers around whether or not it forms via solid-state deformation as a diaplectic glass [Bunch *et al.*, 1967; von Engelhardt and Stöffler, 1968; Hörz and Quaide, 1973], after shear-induced melting [Grady, 1980], or forms via quenching from a melt as a fused glass under high pressure [Chen and El Goresy, 2000]. Solid-state and melting-related formation mechanisms are distinct processes and have different implications for the geochemical behavior of the rock during impact deformation. Most importantly for understanding geochronology, melting and quenching of a fused glass would produce a new material whose age would reflect the time of impact. However, a solid-state mechanism for maskelynite formation needs not necessarily reset isotope systems. Unfortunately, nomenclature is muddled in the literature with maskelynite and diaplectic glass often used interchangeably [Tschermak, 1872; Bunch *et al.*, 1967; Stöffler, 1971; Arndt *et al.*, 1982; Ashworth and Schneider, 1985; White, 1993; Chen and El Goresy, 2000] without clear knowledge of the specific formation mechanism.

Even within these two genetic models (melt versus solid state), the exact formation mechanism is unclear. Multiple hypotheses have been proposed for both static and dynamic compression of silicates. Solid-state models (aka diaplectic glass models) include (1) reversion of high-pressure phases to glass [Ahrens *et al.*, 1969; Williams and Jeanloz, 1988], (2) metamict-like destruction of the order at the unit cell scale [Ashworth and Schneider, 1985], and (3) pressure-induced formation of high-coordination glasses [Hemley *et al.*, 1988].

Models involving melting include (4) shear band-induced melting [Grady, 1977, 1980] and (5) quenching of dense melt under high pressure [Chen and El Goresy, 2000]. Although these models have all been applied to plagioclase [White, 1993], many of the diaplectic glass models, such as formation of high-coordination glass [Ahrens *et al.*, 1969] and metamict-like disruption of the structure at the unit cell scale [Ashworth and Schneider, 1985], are

based on SiO_2 with the assumption that all framework silicates behave similarly. Only a few studies [Hörz and Quaide, 1973; Arndt et al., 1982; Diemann and Arndt, 1984; White, 1993] have specifically focused on plagioclase. Given the additional structural and chemical complexity of the feldspar system compared to SiO_2 , more work focused specifically on this system is warranted.

Previously, a number of analytical and spectroscopic methods have been applied to investigate the structure of maskelynite and other shocked minerals for the purpose of better constraining the formation process. This paper presents an integrated approach using multiple techniques, applying them to the same sample in order to minimize the chance that the samples investigated with each structural tool have seen different extents of shock modification.

2.3. Optical Petrography

Maskelynite, initially identified in the Martian basaltic meteorite Shergotty [Tschermak, 1872], was first described as optically isotropic material derived from plagioclase [Milton and De Carli, 1963; Bunch et al., 1967; Stöffler, 1972]. Petrographically, maskelynite appears similar to plagioclase in plane-polarized light, preserving grain boundaries between maskelynite and pyroxenes such that the texture of the target rock remains. However, the maskelynite has a lower refractive index than unshocked plagioclase. Additionally, in cross-polarized light, maskelynite is easily distinguished from unshocked plagioclase as it is optically isotropic (Figure 1).

2.4. Raman Spectroscopy

Raman spectroscopy, a vibrational spectroscopic technique based on inelastic scattering of monochromatic light, is sensitive to low-frequency lattice modes and is therefore useful for probing mineral crystal structures. As Raman spectroscopy is sensitive to crystallinity, it has been used previously to distinguish and characterize shocked feldspars [Velde and Boyer, 1985; Chen and El Goresy, 2000; Fritz et al., 2005; Jaret et al., 2014].

Crystalline plagioclase has several well-defined Raman active vibrational modes: cation and lattice modes occurring between 200 and 400 cm^{-1} , symmetric T–O–T stretching modes occurring between 500 and 600 cm^{-1} , asymmetric O–T–O bending modes occurring between 600 and 700 cm^{-1} , T–T stretching modes occurring between 700 and 800 cm^{-1} , and T–O stretching modes occurring between 1050 and 1150 cm^{-1} (see Sharma et al. [1983] for complete band assignments). It should be noted that the exact position of these peaks can vary with composition due to the solid solution within the plagioclase series [Mernagh, 1991; Freeman et al., 2008]. Specifically, the strongest and most diagnostic peaks occur near approximately $\sim 509 \text{ cm}^{-1}$, $\sim 485 \text{ cm}^{-1}$, and $\sim 1030 \text{ cm}^{-1}$. These three peaks are useful both for identification of specific feldspar composition [Freeman et al., 2008] and for assessing the level of shock as shown by the decrease in intensity ratio of the 485:509 peaks, merger of these peaks, and significant broadening of the 1030 cm^{-1} peak [Fritz et al., 2005].

2.5. Nuclear Magnetic Resonance Spectroscopy

Solid-state nuclear magnetic resonance (NMR) spectroscopy observes nuclear spin transitions as a way of characterizing local chemical environment [Stebbins and Xue, 2014]. This technique is particularly useful for analysis of amorphous material because it is sensitive only to local environment and not long-range order. Specifically for NMR, the peak position, or chemical shift, of ^{29}Si in silicates is representative of the number and length of Si–O bonds, the types of next nearest neighbor atoms, and other structural features such as Si–O–T bond angles. The peak width reflects the distribution of chemical shifts, providing a measure of disorder, and the area under the peak is proportional to the number of nuclei in that local environment. In silicates, the ^{29}Si chemical shift is most strongly affected by coordination number. Increasing the coordination number (i.e., increasing the mean cation–oxygen distance) generally corresponds to decreasing the chemical shift [Stebbins and Xue, 2014, and references within]. Thus, NMR spectroscopy may be a particularly useful tool for studying shocked material since changes in cation–oxygen distances, increasing coordination number of cations, disordering of materials, and formation of glasses all can occur in response to impact events. NMR spectroscopy utilizing other nuclei, such as ^{27}Al and ^{23}Na in this case, can also provide information on structure in terms of cation–oxygen coordination number. However, peak widths and positions for these nuclei are also affected by nuclear quadrupole effects which complicate interpretation of peak width strictly in terms of disorder. For example, highly distorted sites in otherwise well-crystalline minerals also yield broad peaks, with a

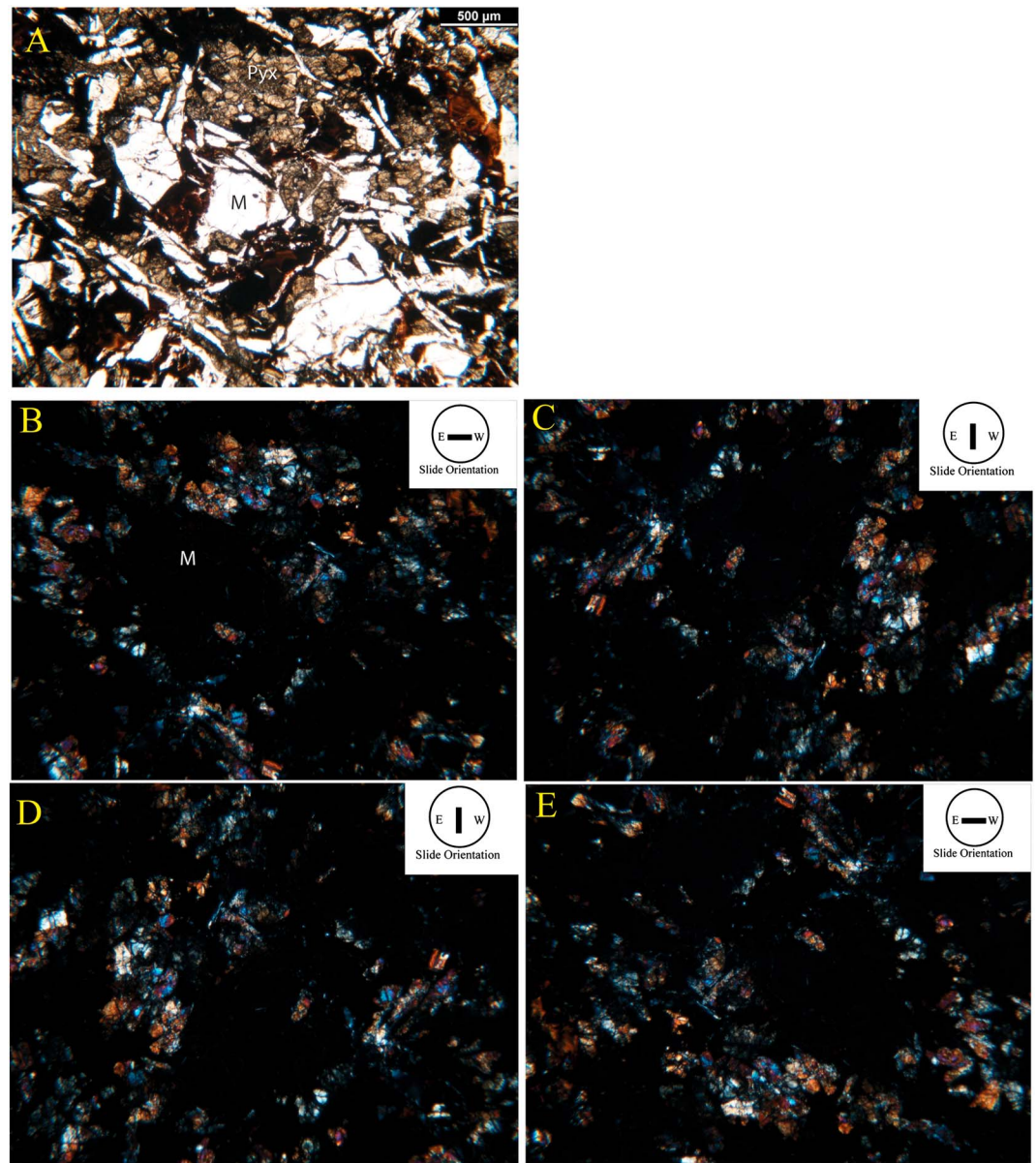


Figure 1. Shocked basalt in thin section under (a) plane polarized light, showing the maskelynite (labeled M) and pyroxenes (labeled pyx). (b–e) Cross-polarized light of the same location of the thin section as Figure 1a, taken at 90° rotations of the microscopy stage. Specific stage orientations are shown in the inset. This sample is thus a low to moderately shocked sample (Class 2) according to the shock classification scheme of Kieffer *et al.* [1976]. Importantly, maskelynite is fully isotropic but no changes are seen in pyroxenes.

width related to the magnitude of quadrupolar coupling (C_q , product of the nuclear quadrupole moment and the largest component of the electric field gradient at the nucleus) and fine structure determined by the departure of the electric field gradient from axial symmetry.

Nuclear magnetic resonance (NMR) spectroscopy of shocked minerals has largely been limited to SiO_2 [Fiske *et al.*, 1998; Boslough *et al.*, 1995; Lee *et al.*, 2012, Yang *et al.*, 1986]. Few studies have investigated feldspar, and these have been primarily focused on the low-shock regime, at pressures below the transition to maskelynite [Cygan *et al.*, 1992]. They report that up to ~22 GPa shock pressures, no systematic changes to Si or Al coordination can be detected. More recently, Lee *et al.* [2012] used ^{27}Al NMR spectroscopy to show that shock compression of a basalt-like diopside-anorthite composition glass produces higher-coordinated Al environments.

2.6. X-Ray Total Scattering

X-ray scattering can be used to determine crystal structure, yielding position of atoms in solids. In contrast to conventional X-ray powder diffraction, which relies solely on Bragg intensities and positions to determine average long-range order, X-ray total scattering experiments collect both Bragg and diffuse scattering and treat them equally. This provides a more direct and precise measurement of interatomic distances and structural order and is particularly useful for amorphous materials which generally lack long-range atomic order (see *Reeder and Michel* [2013] for full technique review). Fourier transforms of total scattering experiments yield a pair distribution function, which represents a distribution of interatomic distances weighted on the basis of scattering power of atom pairs. Pair distribution peaks between 1 and 3 Å is usually interpreted as bond length in the first coordination shell. Peaks between 3 and 4 Å represent distances in the second- and higher-coordination shells. Peaks between 4 and 20 Å represent intermediate range structure associated with connected polyhedral units.

To date, X-ray total scattering experiments have not been applied to shocked materials. Numerous conventional X-ray diffraction studies, however, have been conducted on shocked tectosilicates [*Hanss et al.*, 1978; *Arndt et al.*, 1982; *Ostertag*, 1983; *Diemann and Arndt*, 1984]. These studies show that for both naturally and experimentally shocked samples, the silicate structure collapses with impact pressure [*Hörz and Quaide*, 1973; *Pickersgill*, 2014]. Both Debye-Scherrer (powders) and target micro-X-ray diffraction (XRD) measurements of individual grains show that increasing shock level corresponds to increased asterism and streaking along Debye rings [*Hörz and Quaide*, 1973; *Pickersgill*, 2014]. This breakdown of the crystal lattice is progressive and strongly correlates with shock pressure, and because of this, XRD has been suggested as a tool for analytically quantifying shock pressures [*Hörz and Quaide*, 1973; *Pickersgill*, 2014].

Diemann and Arndt [1984] compared diaplectic glass from the Manicouagan impact structure to a fused glass (at atmospheric pressure) of similar composition. They concluded that there is little structural difference between the fused glass and diaplectic glass. However, they also state that in some cases the diaplectic glass may be slightly less disordered than fused glass. They interpret this to reflect “relics” of crystalline plagioclase preserving long-range order of its former preshock state, as in the shock transformation model of *Grady* [1980]. Alternatively, this could reflect either incomplete or heterogeneous transformation to diaplectic glass, which is commonly seen petrographically at Manicouagan [*Thompson*, 2012].

2.7. Infrared Spectroscopy

Infrared spectroscopy is a particularly useful tool for mineral identification, as the positions and strengths of bands are related to the specific vibrational modes of mineral crystal lattices. Feldspar minerals have absorption bands between 450 and 1200 cm^{-1} reflecting vibrations of (Si,Al) O_4 tetrahedra [*Iiishi et al.*, 1971]. Bending vibrations in the Si–O–Al planar ring occur between 400 and 550 cm^{-1} . Octahedral stretching of SiO_6 occurs between 750 and 850 cm^{-1} , and as minor features between 450 and 700 cm^{-1} . Asymmetric stretching of Si–O occurs between 900 and 1200 cm^{-1} . Contributions from Na–O and Ca–O vibrational modes occur below 450 cm^{-1} [*Iiishi et al.*, 1971; *Johnson et al.*, 2003].

Shock metamorphism, which can cause changes to the refractive index, bond length, and cation coordination number, can cause measureable changes to a mineral's infrared spectrum. For feldspar minerals, *Bunch et al.* [1967] showed that increasing shock corresponds to decreasing spectral detail and decreasing intensity of absorption features. *Stöffler* [1972] and *Stöffler and Hornemann* [1972] showed decreases in the strength of absorption features with increased shock pressure but also showed that band positions shift to lower wave numbers with increased shock. These shifts are believed to be due to the initial formation of amorphous material at about 20 GPa [*Stöffler*, 1972; *Johnson et al.*, 2003].

3. Samples and Methods

3.1. Samples

The samples used in this study were collected at the Lonar crater in 2005, 2006, and winter December 2009 to February 2010 (S. Wright). The Lonar crater, India, is a rare terrestrial impact site, as it is the only terrestrial impact (of ~190 known) emplaced entirely into flood basalt target rocks [*Son and Koeberl*, 2007; Earth Impact Database, 2011] (available at <http://www.passc.net/EarthImpactDatabase/index.html>). The target lithology is a series of basalt flows, ranging in thickness from 5 to 30 m. Only minor petrographic differences

(specifically the number and size of phenocrysts) occur between flows. Mineralogically, these rocks are dominated by 50% labradorite (An_{65}), 31% augite, 7% pigeonite, 8% sulfide and iron-titanium oxides, and 4% other minor phases [Kieffer *et al.*, 1976; Wright *et al.*, 2011]. Texturally, these rocks contain labradorite phenocrysts up to 2 mm in diameter in a fine-grained groundmass (~ 0.2 mm). Shocked samples for this study consist of Class 2 basalt ("LC09-253") [see Wright *et al.*, 2011], which was a clast in the suevite (impact melt-bearing breccia) in the proximal ejecta blanket [Kieffer *et al.*, 1976; Wright *et al.*, 2011; Wright and Newsom, 2013; Wright, 2014]. For comparison to crystalline labradorite, we used samples from Ajanta ("AJ-101"), collected from the Deccan flows, but away from the crater proper [Wright *et al.*, 2011]. For comparison with fused glass we prepared synthetic labradorite glass (An_{60}).

3.2. Methods

For comparison to maskelynite and unshocked labradorite, we synthesized fused glass of labradorite composition. We separated labradorite grains from unshocked Deccan basalts with a Selfrag electromagnetic separator to ensure a pure starting material. A total of 100 mg of separated labradorite grains were heated in a Deltac furnace to 1500°C in a sealed Pt crucible for 90 min before quenching in air.

We conducted optical petrography on polished thin sections. NMR spectroscopy and X-ray total scattering experiments were conducted on powders and on separated single grains of maskelynite. Micro-Fourier transform infrared (FTIR) spectroscopy measurements were conducted on oriented single grains and on polished thin sections. Individual grains were separated using a Selfrag electromagnetic separator at the Lamont-Doherty Earth Observatory and then handpicked under binocular microscopes.

For our electron microprobe analysis, we used the JEOL JXA-8200 Superprobe in the Department of Earth and Planetary Sciences at Rutgers University. Standards included Great Sitkin USNM 137041 anorthite, Kakanui 133868 anorthoclase, NMNH 143966 microcline, Lake County USNM 115900 plagioclase, Tiburon albite, and Kakanui for Fe. All analyses used 15 keV, 15 nA, and a 1 μm spot size, with time dependent integration correction to minimize loss of K and Na.

We collected micro-Raman spectra using a WiTec alpha 300R confocal imaging system, system in the Vibrational Spectroscopy Laboratory at Stony Brook University. It is equipped with a 532 nm Nd YAG laser with 50 mW nominal power at the sample surface and a spot size of 0.76 μm . Each spectrum was acquired through a 50X (0.85 NA) objective and consisted of 60 acquisitions each with a 1 s integration time. All measurements used standard thickness polished thin sections.

We acquired magic-angle spinning (MAS)/NMR spectra for ~ 10 mg of separated maskelynite grains, a sample of crystalline labradorite of similar composition, and fused glass prepared from crystalline labradorite as described above. All samples were contained in 3.2 mm (OD) ZrO_2 rotors. The ^{29}Si spectra were obtained with a 400 MHz (9.4 T) Varian Inova spectrometer operating at 79.4 MHz. We used 3 μs single-pulse excitation ($\pi/2$) and 2 s relaxation delays, corresponding to complete relaxation. Spectra for both ^{27}Al and ^{23}Na were collected with a 500 MHz (11.7 T) Varian InfinityPlus spectrometer operating at 130.3 (^{27}Al) or 132.3 MHz (^{23}Na) at a spinning rate of 20 kHz. The spectra were acquired with 1 μs pulses and 0.2 s relaxation delays, where the nonselective π pulse length was 10 μs ($\nu_{\text{RF}} = 50$ kHz). We also acquired ^{27}Al and ^{23}Na multiple-quantum (multiple quantum magic-angle spinning, MQMAS) spectra of selected samples at 9.4 T and 20 kHz spinning rate. The three-pulse sequence employed excitation and conversion pulses of 2.2 and 0.8 μs for ^{27}Al and 2.9 and 1.1 μs for ^{23}Na ($\nu_{\text{RF}} = 120$ kHz), and a 15 μs selective 90° zero-quantum filter pulse. The isotropic dimension was sampled with 20–36 points incremented by 25 μs (40 kHz spectral window in F1) using hypercomplex phase cycling for a total of 2400–9000 acquisitions.

High-energy X-ray total scattering experiments used 10 mg of picked maskelynite grains, fused glass of labradorite composition, and single maskelynite grains in different orientations. Two-dimensional diffraction data were collected on a Perkin-Elmer XRD 1621 detector at the beamlines 11-ID-B at the Advanced Photon Source and X17B3 at the National Synchrotron Light Source at wavelengths of 0.2128 Å and 0.1529 Å, respectively. The background from the Kapton capillary and the hutch was measured and subtracted from the exposures containing the sample. Fit2D was used for the determination of the geometric parameters and the radial integration of the two-dimensional data [Hammersley *et al.*, 1996]. The total scattering function $S(Q)$, which is the measured and normalized scattering intensity from the sample, was obtained using the program PDFgetX2 [Qiu *et al.*, 2004] where standard corrections were applied as well as those unique to

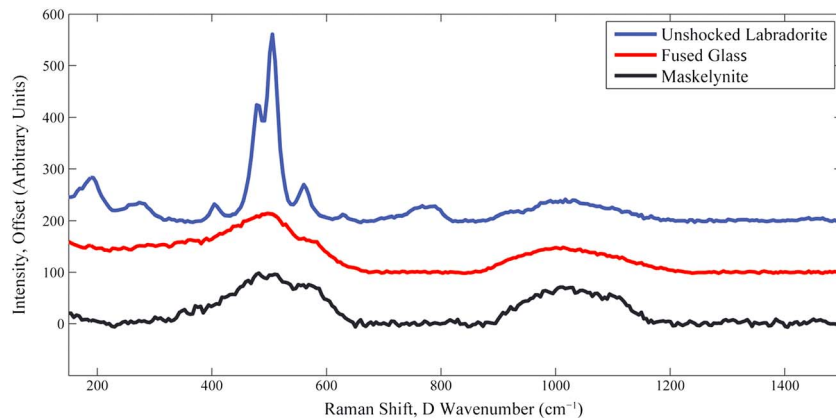


Figure 2. Micro-Raman spectra of (top line, blue) unshocked labradorite, (middle line, red) fused glass, and (bottom line, black) maskelynite. Only the unshocked labradorite shows strong, narrow peaks. Both fused glass and maskelynite exhibit only broad peaks near 496 and 1030 cm^{-1} .

area-detector geometry [Chupas *et al.*, 2003]. The pair distribution function $G(r)$ was generated by direct Fourier transformation of $S(Q)$ with a Q_{max} of 22 \AA^{-1} .

We collected micro-FTIR point spectra of single grains in thin section using a Nicolet iN10MX FTIR microscope, in the Vibrational Spectroscopy Laboratory at Stony Brook University. This instrument is equipped with a liquid nitrogen-cooled HgCdTe array detector capable of acquiring hyperspectral image cubes between 715 and 7000 cm^{-1} (1.4–14 μm) at 25 $\mu\text{m}/\text{pixel}$ spatial sampling. To test for spectral isotropy, single grains of maskelynite were individually mounted in an epoxy puck, and the single grain was then rotated 90° to obtain a second measurement of the grain. This was repeated with three different grains. A similar method was used for crystalline labradorite and fused glass.

4. Results

4.1. Optical Petrography

In plane-polarized light, Lonar maskelynite occurs as phenocrysts and within the groundmass. Maskelynite appears uniformly smooth, lacking planar deformation features (PDFs), and planar fractures. Both phenocrysts and grains within the groundmass are euhedral to subhedral and show no textural evidence of melting (Figure 1a). In cross-polarized light, maskelynite grains remain at extinction through complete 360° rotation of the microscope stage (Figures 1b–1e). No remnant or partial birefringence was observed. Pyroxenes, however, appear unaffected by shock, showing typical interference colors, and lack fracturing or granularization that is commonly reported for highly shocked basalts.

Based on optical shock classification schemes, these samples are low to moderate shock, Class 2 [Kieffer *et al.*, 1976] or Stage I [Stöffler, 1971], indicating shock pressures between 25 and 28 GPa, as suggested by only minor cracking of adjacent pyroxenes [Kieffer *et al.*, 1976; Stöffler, 1971].

4.2. Micro-Raman Spectroscopy

As shown in Figure 2, unshocked labradorite exhibits characteristic peaks at 190, 482, 505, and 561 cm^{-1} and lower intensity peaks at 270, 406, and 778 cm^{-1} , and a slight peak centered near 1030 cm^{-1} . Fused labradorite glass exhibits two broad peaks at 495 and 1025 cm^{-1} , with full width at half maximum (FWHM) of 169 and 138 cm^{-1} respectively. There is also a slight shoulder at 559 cm^{-1} . Maskelynite also exhibits two broad peaks at 482 and 1012 cm^{-1} , with FWHM of 174 and 189 cm^{-1} , respectively, and a slight shoulder at 559 cm^{-1} .

4.3. NMR Spectroscopy

NMR spectra and peak parameters for ^{29}Si , ^{27}Al , and ^{23}Na are shown in Figure 3 and Table 1. The NMR spectra of Lonar maskelynite contain broad, featureless peaks that document an increase in the short-range disorder beyond the first coordination sphere. For example, the ^{29}Si spectrum of maskelynite (Figure 3a) shows a

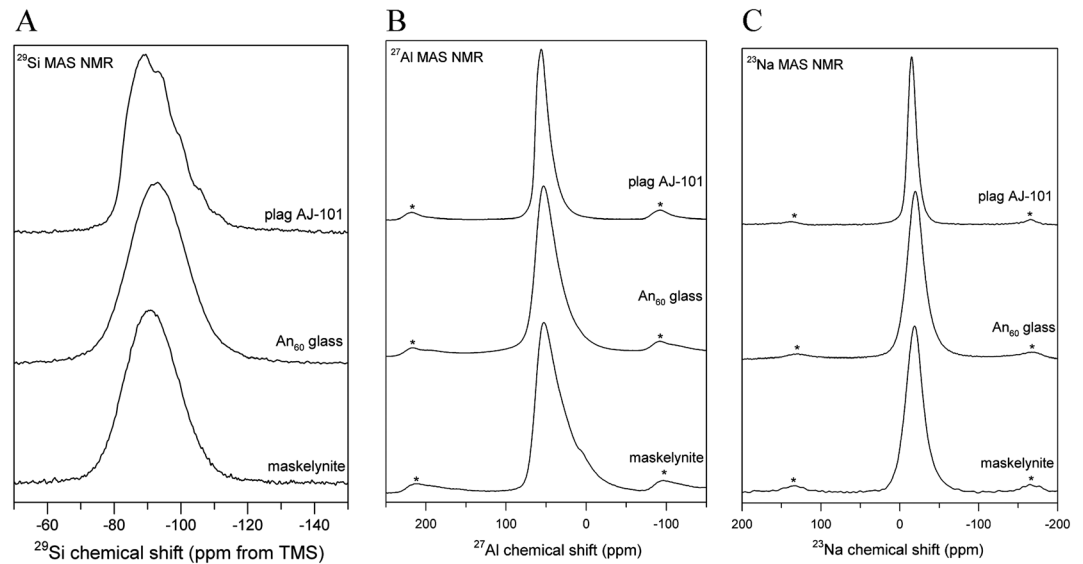


Figure 3. Comparison of (a) ^{29}Si , (b) ^{27}Al , and (c) ^{23}Na NMR spectra of maskelynite (bottom), An63 composition fused glass (middle), and crystalline laboradorite. Corresponding spectral line shape parameters are presented in Table 1. For ^{29}Si , ^{27}Al , and ^{23}Na , maskelynite is clearly less ordered than the crystalline laboradorite. The ^{29}Si peak is slightly narrower than that for fused glass. The opposite is true for ^{27}Al and ^{23}Na , where maskelynite shows a slightly broader peak than fused glass. Asterisks denote positions of spinning sideband artifacts. Spectra are plotted as relative frequency shifts (parts per million, ppm) from standard reference materials tetramethylsilane (^{29}Si) and 0.1 m solutions of AlCl_3 (^{27}Al) and NaCl (^{23}Na).

broad, approximately Gaussian-shaped peak for four-coordinated Si centered near -91 ppm with a width of 18.6 ppm FWHM. We found no evidence for five- or six-coordinated Si (chemical shift range approximately -150 to -220 ppm) in this spectrum nor in several others that were taken over extended periods and at both short and long relaxation delays (0.2 to 120 s) under conditions optimized to detect such species. In comparison, the spectrum of crystalline, unshocked laboradorite is asymmetric and contains fine structure from resolution of distinct crystallographic sites and local environments with differing numbers of adjacent framework Al atoms. This spectrum is typical for those of intermediate composition plagioclase feldspars [Kirkpatrick *et al.*, 1985], for which the signal is broad due to a wide range of chemical shifts for the different crystallographic sites and poorly resolved owing to short-range disorder in the occupancy of adjacent tetrahedral sites (i.e., Si–O–(Si,Al)). Surprisingly, the overall width and average chemical shift of the maskelynite peak is otherwise similar to those for the crystalline laboradorite, indicating absence of large differences in the structure such as in the polymerization of the silicate tetrahedra. The average chemical shift is about 1.5 ppm higher for maskelynite, which can be interpreted as a small decrease in the average Si–O–T angle, of about 3° [e.g., Mauri *et al.*, 2000]. The slightly broader peak for maskelynite, by about 1 ppm, likewise can be interpreted as an increase in the range of Si–O–T bond angles. In contrast, the fused laboradorite composition glass yields a peak that is broader (3 ppm) than that for maskelynite with an average chemical shift that is shifted to slightly lower chemical shift compared to the crystalline laboradorite.

Table 1. Peak Position, Weighted Average Chemical Shift (M1), and Width (Full Width at Half Maximum; FWHM) of NMR Spectra Obtained for Crystalline Plagioclase, Fused An₆₀ Composition Glass, and Maskelynite^a

	^{29}Si			^{27}Al			^{23}Na		
	Peak	M1	FWHM	Peak	M1	FWHM	Peak	M1	FWHM
Plag	-89.5^b	-92.7	17.6	56.0^b	50.8	18.9	-14.9	-16.4	12.8
An60	-93.0	-93.0	20.0	53.3	44.9	31.2	-19.7	-21.4	24.3
Maskelynite	-91.1	-91.1	18.6	52.7	37.8	36.5	-18.6	-20.0	25.0

^aAll values in ppm. Data for Al and Na are values observed at 11.7 T, uncorrected for quadrupolar, broadening, and shifts.

^bPosition of most prominent peak, several peaks present in the fine structure.

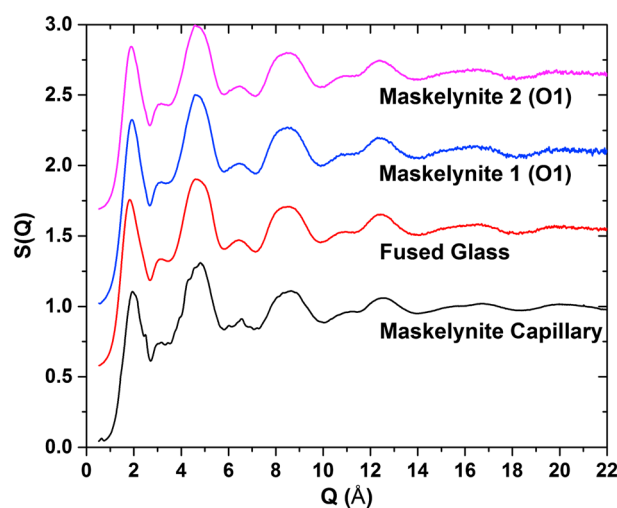


Figure 4. Structure factor $S(Q)$ of four different maskelynite samples—two single maskelynite grains, assorted maskelynite grains in a capillary, and a fused glass with An_{60} composition. Even despite compositional differences between maskelynite (An_{63}) and the fused glass (An_{60}), the different samples are undistinguishable on the basis of the structure factor.

Likewise, the ^{27}Al and ^{23}Na NMR spectra show evidence for peak broadening associated with disorder in maskelynite (Figures 3b and 3c), although these data are less easily related directly to structural differences. The ^{27}Al NMR spectrum contains a broad asymmetric peak with a sharper edge at high chemical shifts and a broad tail extending to negative chemical shifts. This peak shape is characteristic of a range of quadrupolar coupling constants (C_q) arising from dispersion of electric field gradients at the nucleus [Coster *et al.*, 1994; d'Espinose de Lacaillerie *et al.*, 2008]. The chemical shifts correspond approximately to the left edge of the spectrum, approximately 60 ppm, and are characteristic of four-coordinated Al in a framework structure. The peak position is a complex function of the distribution of quadrupolar coupling constants and cannot be easily interpreted

from these results. Although the broad tail overlaps the chemical shift range for six-coordinated Al (near 0 ppm), the MQMAS spectrum (not shown) shows conclusively that nearly all of this signal intensity arises from tetrahedral Al having large peak width due to large C_q values. An additional, small feature occurs near +10 ppm, in the range for octahedral Al. The intensity of this shoulder varied among subsamples suggesting that it could arise from an impurity, such as a clay mineral. The MQMAS data also contain evidence for the presence of a small amount of six-coordinated Al in the sample (<1%), but we could not ascertain with certainty whether this higher-coordinated Al arises from the maskelynite or an impurity phase.

Comparison of the maskelynite ^{27}Al NMR spectrum with those obtained for crystalline laboradorite and laboradorite composition glass shows a progression in the extent of the low-frequency tail and hence increases in the range of electric field gradients from crystalline to fused glass to maskelynite (Figure 3b). Structurally, the electric field gradient relates to departure from cubic symmetry, which to first order can be associated with distortion of the Al coordination polyhedron from a perfect tetrahedron (although longer-range factors also contribute). The Al tetrahedra in crystalline feldspars depart from tetrahedral symmetry, giving rise to the breadth and asymmetry of the peak for crystalline laboradorite, but the extent of the local distortions is clearly much greater in maskelynite.

The MAS NMR results for ^{23}Na (Figure 3c) are somewhat similar to those for ^{27}Al in that the line shapes are also affected by quadrupolar effects and show progressively larger width from crystalline laboradorite to fused glass to maskelynite. The ^{23}Na spectrum of maskelynite is more symmetrical than that for ^{27}Al , as shown by the similarity of the peak position (−18.6 ppm) and average chemical shift (−20 ppm), suggesting that the peak width is less influenced by distribution of electric field gradients. The MQMAS data (not shown) indicate that much of the peak width can be attributed to a range of chemical shifts, which can be interpreted as dispersion in the weighted average Na–O bond distances [Angeli *et al.*, 2000]. Taken together, the NMR spectra show that the structural disorder in maskelynite affects the local environment of both the framework cations and Na.

4.4. High-Energy X-Ray Total Scattering

The structure factor $S(Q)$ of the different maskelynite grains and the fused glass (An_{60}), and multiple maskelynite grains in a capillary are shown in Figure 4. On basis of the structure factor, the samples of single maskelynite and fused glass grains are indistinguishable, while the assortment of grains in the capillary shows signs of some crystalline contribution. The minor crystalline phase in the capillary data was identified as plagioclase, suggesting that some or parts of the separated grains were crystalline plagioclase. The pair distribution

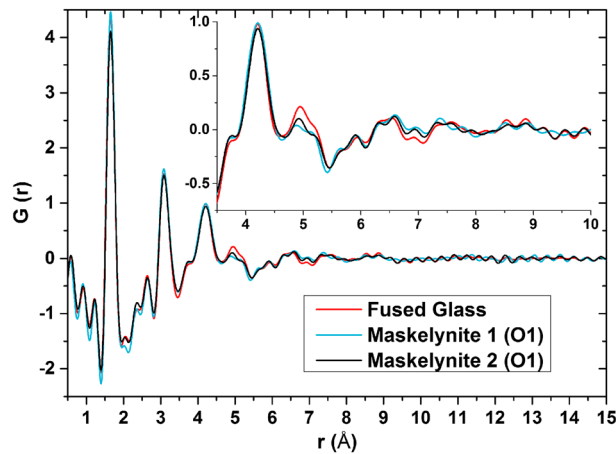


Figure 5. The pair distribution function $G(r)$ of two different maskelynite grains and fused glass. The inset shows the region characteristic for the intermediate range order in the atomic arrangement.

1980] indicating a modification or breakup of the ordered tetrahedral crankshaft structure in crystalline plagioclase. The range in the pair distribution function between 4 and 10 Å provides insight into the connectivity of the local structure motif. Here a significant difference of the intermediate range order can be observed between the maskelynite samples and the fused glass (inset Figure 5). The two maskelynite grains show a larger number of resolved maxima in the intermediate range in the $G(r)$, compared with the $G(r)$ of the fused glass. This indicates that in maskelynite the intermediate range distances (4–10 Å) and dihedral angles have a narrower distribution, which represents an increased degree of atomic order. In comparison, the atomic arrangements in fused glasses can be described as continuous random network leading to a broad dihedral angle and distance distribution, which manifest as broader maxima in the pair distribution function $G(r)$.

Figure 6 shows the $G(r)$ of maskelynite grain 1 collected at a different orientations randomly, rotated 90° from the first. The pair distribution function, $G(r)$, is distinctively different between the two orientations, potentially showing a remnant of anisotropy otherwise only observed in crystalline samples.

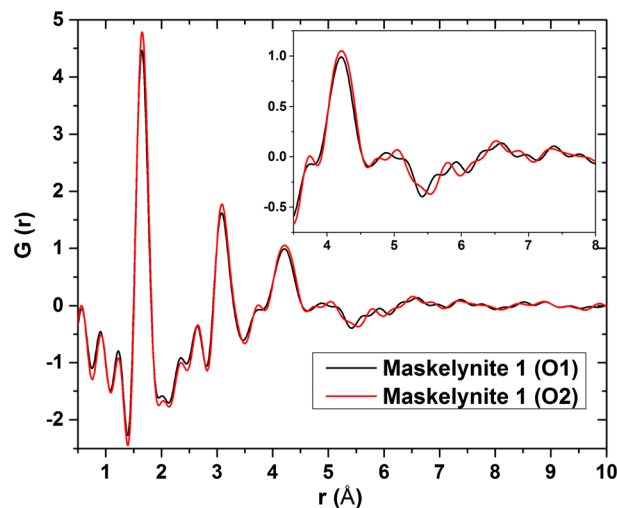


Figure 6. The pair distribution function $G(r)$ of two different orientations of a single maskelynite grain. The inset shows the region characteristic for the intermediate range order in the atomic arrangement.

functions, $G(r)$, of the maskelynite grains and fused glass are shown in Figure 5. The largest correlations observed in the $G(r)$ for all investigated samples are less than 10 Å, similar to the unit cell parameters for one unit cell in plagioclase [Wenk *et al.*, 1980]. Therefore, it can be concluded that maskelynite is an amorphous solid and not nanocrystalline. The local region of the pair distribution function of maskelynite samples and the fused glass are similar. All show a maximum at 1.6 Å and 3 Å characteristic for Si–O distances in tetrahedral and the intertetrahedral Si–Si distance. The Si–Si distance in maskelynite and the fused glass is shorter than the Si–Si distances in crystalline labradorite [Wenk *et al.*,

4.5. Micro-FTIR Spectroscopy

Unshocked labradorite from the Deccan region exhibits two primary peaks between 700 and 1300 cm^{-1} , dependent upon orientation, as typical for labradorite [Rucks *et al.*, 2015]. The first peak is centered at 900 or 1001 cm^{-1} , and the second peak is centered between 1100 and 1175 cm^{-1} . However, at orientation 2, a small shoulder also develops near 990 cm^{-1} in addition to a peak near 900 cm^{-1} (Figure 7a). The fused glass of labradorite composition exhibits one peak centered at 995 cm^{-1} , the position of which is independent of orientation (Figure 7b).

Maskelynite exhibits one broad peak compared to two narrower peaks typical of crystalline labradorite. The peak position varies by nearly 40 cm^{-1} depending upon orientation. For orientation 1, the peak

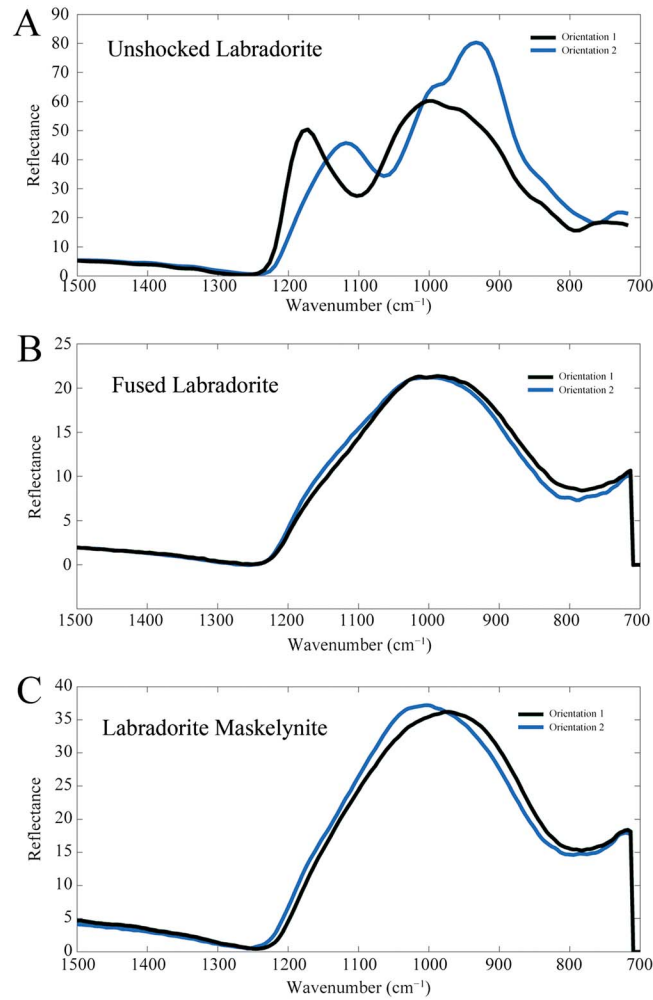


Figure 7. Micro-FTIR spectra of rotated samples. For each analysis, the sample was mounted in an epoxy mount, and the entire block was rotated 90° to obtain measurements of multiple orientations through the sample. (a) unshocked labradorite, (b) fused glass of labradorite composition, and (c) maskelynite (of labradorite composition). Rotating unshocked labradorite corresponds with shifts in peak positions from 1175 cm^{-1} and 1001 cm^{-1} to 1110 cm^{-1} and 920 cm^{-1} with a shoulder at 990 cm^{-1} . Fused glass has only one peak at 995 cm^{-1} , independent of orientation. Maskelynite has one peak, but upon rotation the peak position changes from 1000 cm^{-1} to 960 cm^{-1} .

within labradorite) and because of differences in technique (emissivity measurements of chips and powders compared to IR reflectance of individual grains).

5. Discussion

5.1. Comparison of Maskelynite to Fused Glass and Crystalline Labradorite

Raman spectroscopy reveals that maskelynite is distinctly different from the crystalline labradorite, with a spectrum nearly identical to that of fused glass (Figure 2). There are slight differences between the maskelynite and the fused glass in both peak position and intensity. Fused glass shows a higher intensity of the 495 cm^{-1} peak compared to the background. However, this is a minor effect and may simply reflect nonstructural sample differences, such as quality of the surface polish. The position of the fused glass and maskelynite peaks near 495 cm^{-1} appears offset, but given the broad nature of these peaks, this difference in peak center may not be indicative of a compositional or structural difference. The pattern

position was centered at 960 cm^{-1} , whereas after being rotated to an orientation perpendicular to the first measurement, the peak position is centered at 1000 cm^{-1} (Figure 7c). All three grains measured showed similar behavior.

We investigated the magnitude of changes in micro-FTIR peak position as a function of composition by performing an electron microprobe analysis of the same individual grains measured with micro-FTIR. A comparison of peak position with An# is shown in Figure 8 and Table 2, where variations in peak position over the compositional range An₆₂ to An₆₉ are not well correlated. For example, the eight grains of An₆₄ range in peak position from 987 cm^{-1} to 1034 cm^{-1} . The five grains of An₆₅ range in peak position from 995 cm^{-1} to 1030 cm^{-1} . Although we only have two measurements of grains with An# less than 62, we suggest a similar pattern would exist with a great sample size. Therefore, the implication is that these differences in peak position reflect the varying orientations of the grains in the rock more than any minor compositional variations in the samples.

This interpretation is slightly different from previous work [Johnson, 2012] which concluded there are correlations between IR peak position and both composition and shock level. These data, however, may not be directly comparable because of differences in range of compositional variability (differences between albite and bytownite compared to variation

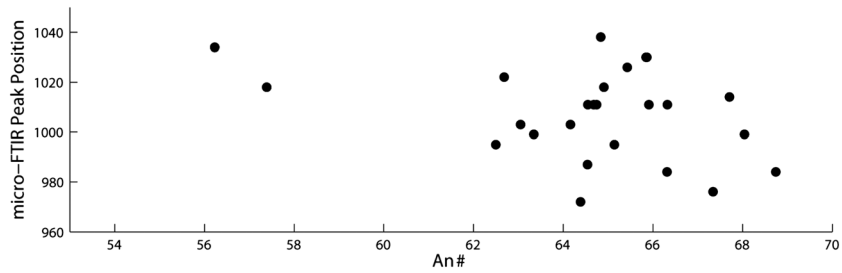


Figure 8. Composition (plotted as An #) of maskelynite compared to micro-FTIR peak position of grains measured in thin section. Each point represents a different grain in thin section. All grains are fully isotropic at visible wavelengths. The shifts in peak position does not correspond to changes in An # but are consistent with shifts due to orientation as shown in Figure 7c. Although we do not know the orientation of these grains in the thin section, we attribute the difference in peak position of different grains to reflect a preservation of intermediate order in the maskelynite.

of two broad peaks centered near 495 cm^{-1} and 1025 cm^{-1} is also consistent with Raman patterns of synthetic fused glass of various plagioclase compositions [Sharma *et al.*, 1983]. It should be noted, however, that we encountered one example of slight heterogeneity in the fused glass, suggesting there may have been minor areas that retained minor remnant crystallinity. As noted earlier by Treiman and Treado [1998] and confirmed here, Raman spectroscopy alone is insufficient for distinguish impact melt glass (i.e., fused glass) from maskelynite despite common use for this purpose [Chen and El Goresy, 2000].

NMR results for ^{29}Si show that both fused glass and maskelynite yield just one symmetric peak, rather than an asymmetric partially resolved spectrum typical of crystalline laboradorite (Figure 3), indicating absence of long-range order. The spectra of fused glass and maskelynite also differ; the peak for fused glass is 3 ppm broader than for maskelynite, and the average peak position is in the opposite direction from that for crystalline laboradorite. These observations suggest that in terms of the range of Si–O–T bond angles maskelynite is more similar to crystalline laboradorite than fused glass. In contrast, the broader ^{27}Al and ^{23}Na NMR signals from

maskelynite indicate more distortion of the local coordination polyhedra. These differences between maskelynite and fused glass likely reflect differences in formation mechanism. Disordering by short-range atomic displacements would be expected to largely preserve the feldspar framework topology in terms of ring structure and range of Si–O–T angles, but could lock-in high-energy distortions of the coordination polyhedra, whereas quenched melt would contain a more random aluminosilicate network structure but lower energy local bonding configurations. Both composition and quenching rate can affect peak, width, and position, but here the maskelynite and synthetic fused glass are compositionally similar (An_{60} versus An_{63}) and quenching of our synthetic fused glass was done very rapidly, ensuring high-energy local bonding configurations. We suggest that these differences between fused glass and maskelynite are reflecting differences in the style of structural disorder.

Table 2. Comparison of Maskelynite Peak Position and Specific Composition Shown in Figure 8

Grain	An #	FTIR Peak Center
1	56.23	1034
2	57.39	1018
3	62.5	995
4	62.68	1022
5	63.05	1003
6	63.34	999
7	64.16	1003
8	64.39	972
9	64.54	987
10	64.55	1011
11	64.68	1011
12	64.74	1011
13	64.84	1038
14	64.91	1018
15	65.14	995
16	65.43	1026
17	65.85	1030
18	65.86	1030
19	65.91	1011
20	66.31	984
21	66.32	1011
22	67.34	976
23	67.71	1014
24	68.04	999
25	68.74	984

Recently, Lee *et al.* [2012] showed NMR evidence for shock-induced changes to Al coordination in experimentally shocked fused glasses. They showed that after shock the ^{27}Al peak center moves toward a more negative chemical shift and the peak width increases and is associated with small amounts of higher-coordination Al. Although our maskelynite does show some six-coordinated Al, this might alternatively reflect a minor clay component, which is common in weathered plagioclase. This observation is consistent with the ^{29}Si NMR results discussed above.

The X-ray total scattering data show similarity on the length scale of the local structure between fused glass and maskelynite (Figure 4). Here we compared maskelynite of An_{63} composition to fused glass of labradorite (An_{60}) composition. Despite the minor compositional differences, there is no detectable difference in $S(Q)$ between the fused glass and the maskelynite.

However, significant differences in the number and location of discrete maxima are observed in the intermediate range of the pair distribution function $G(r)$ between fused glass and maskelynite. Maskelynite shows a higher degree of intermediate range order compared to fused glass (Figures 5 and 6).

Importantly, the residual anisotropy in the atomic arrangement of maskelynite observed in the $G(r)$ of the same maskelynite grain in different orientations suggests that maskelynite is not formed through a melting process but rather through direct amorphization from a crystalline phase that preserves some of the framework topology. If maskelynite did form through a melting process, the $G(r)$ obtained for maskelynite in two different orientations (Figure 6) would be identical, as it is expected for an isotropic solid such as fused glasses.

Although these maskelynite grains are optically isotropic at visible wavelengths, the orientation-dependent infrared reflectance peak position (Figure 7) suggests that the maskelynite is not isotropic in the infrared. We replicated the IR experiments for three individual grains, and the results shown in Figure 7 represent the measurements taken at as close to 90° as possible. It should be noted, however, that the exact value of this peak position shift can vary depending on how the specific crystallographic orientations are measured. For orientations that are less than 90° apart, we measured differences in peak position of 40 and 60 cm^{-1} . Importantly, the exact value of difference in peak position is less diagnostic than the presence of shifting.

Similarly, we interpret the variation of peak position of maskelynite grains in thin section to also be due to orientation. Electron microprobe analysis of the same individual grains measured with micro-FTIR indicates no compositional dependence on peak position for these samples with limited compositional variation between An_{62} and An_{69} (Figure 8). For example, two grains of An_{65} have micro-FTIR peak positions of 1026 and 995 cm^{-1} . Similarly, two maskelynite grains with micro-FTIR peak positions of 1018 cm^{-1} have $\text{An}\#$ s of 57 and 64. Since we established there is no direct correlation between peak position and $\text{An}\#$ in these samples, it is therefore highly likely that the difference in peak position reflects the random orientations of the grains in the rock.

Previous infrared studies of maskelynite [Ostertag, 1983; Johnson *et al.*, 2003] concluded that the spectrum of maskelynite was indistinguishable from the spectrum of fused glass. These studies differ from ours in that they measured powders and rock chips of larger samples, which included multiple grains at random orientations, rather than individual grains, resulting in an averaged orientation reflected in the spectra. By measuring multiple orientations of single grains, we show that maskelynite is amorphous yet not necessarily isotropic at all wavelengths in the infrared.

The cause of anisotropy of maskelynite at infrared but not at visible wavelengths remains somewhat perplexing, but we offer two possible explanations. First, this could be due to a difference in sensitivity of the instruments—traditional polarizing light microscope and human eyes for visible light versus an HgCdTe array detector for the infrared. Perhaps, the IR detector is simply more sensitive and is able to detect changes that are not resolvable with our eyes.

Alternatively, and more likely, this anisotropy could be related to how the shock process affects the refractive index during transformation from plagioclase to maskelynite. In visible light, the maximum difference in refractive index with orientation is small compared to that at IR wavelengths. Perhaps, during maskelynite formation, the difference in refractive index with orientation decreases in such a way that at visible wavelengths there is no difference but at IR wavelengths, which start out with a large refractive index, there still remains a detectable difference with orientation.

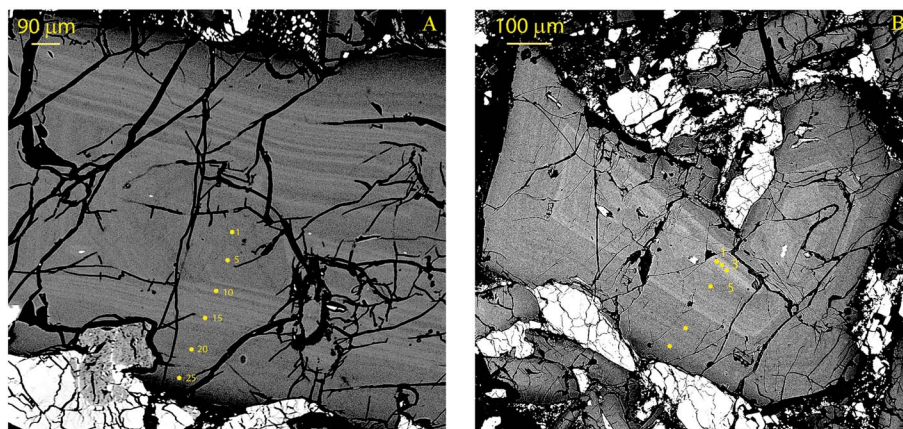


Figure 9. (a and b) Backscattered electron images of two maskelynite grains. Compositional data are shown in Table 3, with analysis locations indicated by yellow dots. Even though the maskelynite is optically isotropic, strong oscillatory zoning (Figure 9a) is preserved.

Anisotropy at X-ray wavelengths is easier to explain. We attribute this to maskelynite formation by short-range atomic displacements, leaving some of the atomic-scale feldspar topology mostly intact. Unlike the visible and IR anisotropy, our X-ray analyses do not rely on reflectance and probe the atomic distances directly.

Our X-ray results are different from previous X-ray studies that used powders [Ostertag, 1983] or unoriented micro-XRD [Pickersgill, 2014]. Neither of the previously used techniques would be capable of detecting anisotropy because powders average orientation effects and analyses of a single orientation in thin section are not sufficient to detect anisotropy.

Importantly, the maskelynite grains in this study also show the preservation of original preshock igneous crystallization textures, as illustrated by the presence of oscillatory compositional zoning (Figure 9). The preservation of feldspar stoichiometry (Table 3) suggests that the transformation from labradorite to maskelynite was not accompanied by geochemical changes or diffusive loss of light elements such as Ca, Na, and K.

Zoning in terrestrial maskelynite has only been briefly noted from Lonar [Fredriksson *et al.*, 1979]. Martian maskelynite, on the other hand, has received considerably more discussion. Zoning from $An_{54}Ab_{44}Or_2$ to $An_{42}Ab_{54}Or_4$ has been reported in Shergotty and nearly identical $An_{55}Ab_{43}Or_2$ to $An_{43}Ab_{53}Or_4$ is seen in Zagami, and maskelynite from EETA 79001 shows oscillatory zoning [Treiman and Treado, 1998; Milkouchi *et al.*, 1999]. Such preservation of zoning has been used to argue that this meteoritic maskelynite formed via solid-state processes. Similarly, we find it difficult to envision a scenario where melting would preserve this texture because of likelihood of cations, especially Na, diffusing during melting and subsequent cooling.

The use of zoning in maskelynite as an indicator of solid-state deformation has been challenged by Chen and El Goresy [2000], who claim that zoning in Shergotty maskelynite is restricted to partially birefringent grains and those with Raman patterns indicative of crystalline (or partially crystalline) material. They, therefore, argue that the zoning in Shergotty maskelynite reflects a region of the sample that has not experienced as high shock pressures. However, this is not the case for our samples, as the same sample that exhibits preserved zoning has a Raman pattern consistent with an amorphous material (Figure 2).

Our results highlight the importance of a multitechnique approach. Any technique—particularly either Raman or unoriented infrared or X-ray techniques—may be insufficient to properly distinguish crystalline plagioclase, maskelynite, and fused plagioclase composition glass. Our analyses suggest that shock-produced maskelynite “glass” is fundamentally different from fused glass because fused glass does not show any effect of orientation. For maskelynite, we suggest these grains formed by short-range atomic displacements rather than melting without internal homogenization resulting from long-range or diffusive movement of atoms within the grain. Such a formation mechanism is consistent with the observed preservation of grain boundaries and zoning of the maskelynite and lack of flow textures, suggesting a formation mechanism purely via solid-state transformation [Stöffler, 1971; Hörz and Quaide, 1973] not through quenching of a higher pressure melted glass [Chen and El Goresy, 2000; El Goresy *et al.*, 2013].

Table 3. Chemical Composition of Maskelynite Grains Shown in Figure 9^a

Spot	SiO ₂	Al ₂ O ₃	CaO	FeO	Na ₂ O	K ₂ O	Total	An #	Formula Units Ca	Formula Units Na	Formula Units K	Formula Units Fe	Formula Units Al	Formula Units Si	Formula Units Ca + Na + K	Formula Units Fe + Al + Si
<i>Grain A</i>																
1	51.84	30.67	13.72	0.60	3.89	0.14	100.86	65.57	0.66	0.34	0.01	0.02	1.63	2.34	1.01	4.00
2	51.78	30.79	13.63	0.52	3.55	0.18	100.46	67.24	0.66	0.31	0.01	0.02	1.64	2.35	0.98	4.01
3	51.54	30.57	13.61	0.54	3.31	0.16	99.71	68.80	0.66	0.29	0.01	0.02	1.64	2.35	0.97	4.01
4	51.47	30.87	13.66	0.57	3.73	0.11	100.40	66.51	0.66	0.33	0.01	0.02	1.65	2.34	1.00	4.01
5	51.33	30.84	13.67	0.53	3.70	0.13	100.21	66.61	0.67	0.33	0.01	0.02	1.65	2.33	1.00	4.01
6	51.35	30.57	13.54	0.57	3.45	0.17	99.64	67.75	0.66	0.31	0.01	0.02	1.65	2.35	0.98	4.01
7	51.27	30.64	13.45	0.52	3.33	0.11	99.31	68.59	0.66	0.30	0.01	0.02	1.65	2.35	0.96	4.02
8	51.46	30.62	13.60	0.52	3.51	0.13	99.85	67.62	0.66	0.31	0.01	0.02	1.64	2.35	0.98	4.01
9	50.91	31.06	13.83	0.55	3.23	0.12	99.70	69.78	0.68	0.29	0.01	0.02	1.67	2.32	0.97	4.02
10	51.49	30.53	13.35	0.50	3.73	0.15	99.73	65.84	0.65	0.33	0.01	0.02	1.64	2.35	0.99	4.01
11	50.15	31.51	14.57	0.54	3.04	0.09	99.91	72.20	0.71	0.27	0.01	0.02	1.70	2.29	0.99	4.01
12	50.32	31.35	14.35	0.52	3.33	0.10	99.97	69.98	0.70	0.30	0.01	0.02	1.69	2.30	1.00	4.01
13	50.12	31.63	14.51	0.56	3.23	0.14	100.20	70.71	0.71	0.29	0.01	0.02	1.70	2.29	1.00	4.01
14	51.07	30.79	13.78	0.53	3.44	0.16	99.77	68.24	0.67	0.30	0.01	0.02	1.66	2.33	0.99	4.01
15	50.48	31.49	14.50	0.54	3.52	0.12	100.65	69.00	0.71	0.31	0.01	0.02	1.69	2.29	1.02	4.00
16	50.39	31.37	14.23	0.55	3.07	0.11	99.72	71.41	0.70	0.27	0.01	0.02	1.69	2.30	0.98	4.01
17	51.56	30.45	13.43	0.56	3.68	0.14	99.81	66.31	0.66	0.33	0.01	0.02	1.64	2.35	0.99	4.01
18	51.47	30.52	13.49	0.62	3.67	0.14	99.92	66.43	0.66	0.32	0.01	0.02	1.64	2.35	0.99	4.01
19	51.68	30.25	13.35	0.64	3.46	0.14	99.53	67.50	0.65	0.31	0.01	0.02	1.63	2.36	0.97	4.01
20	51.94	30.06	13.00	0.63	3.85	0.16	99.64	64.47	0.64	0.34	0.01	0.02	1.62	2.37	0.99	4.01
21	52.16	30.00	13.06	0.66	3.74	0.14	99.75	65.31	0.64	0.33	0.01	0.03	1.61	2.38	0.98	4.01
22	52.18	29.98	12.83	0.67	3.95	0.16	99.78	63.61	0.63	0.35	0.01	0.03	1.61	2.38	0.98	4.01
23	52.06	30.17	13.27	0.67	3.83	0.15	100.16	65.08	0.65	0.34	0.01	0.03	1.62	2.37	0.99	4.01
24	52.55	29.66	12.52	0.70	3.97	0.14	99.54	63.02	0.61	0.35	0.01	0.03	1.59	2.40	0.97	4.02
25	53.85	28.98	11.73	0.80	4.29	0.20	99.84	59.47	0.57	0.38	0.01	0.03	1.55	2.44	0.96	4.02
26	56.15	27.74	10.53	0.80	5.16	0.29	100.67	52.09	0.51	0.45	0.02	0.03	1.47	2.52	0.97	4.01
27	58.82	26.94	9.16	0.89	5.95	0.40	102.14	44.90	0.43	0.51	0.02	0.03	1.40	2.59	0.96	4.02
<i>Grain B</i>																
1	51.25	33.10	15.32	0.57	2.68	0.07	102.99	75.68	0.73	0.23	0.00	0.02	1.73	2.27	0.96	4.02
2	50.69	33.27	15.47	0.66	2.60	0.07	102.76	76.32	0.74	0.22	0.00	0.02	1.74	2.25	0.97	4.02
3	48.90	32.32	15.25	0.55	2.77	0.08	99.88	74.90	0.75	0.25	0.00	0.02	1.75	2.24	1.00	4.01
4	51.17	30.52	13.57	0.55	3.51	0.12	99.45	67.61	0.67	0.31	0.01	0.02	1.65	2.34	0.98	4.01
5	51.43	30.39	13.40	0.61	3.66	0.14	99.64	66.36	0.66	0.32	0.01	0.02	1.64	2.35	0.99	4.01
6	53.55	29.56	12.20	0.80	4.22	0.21	100.54	60.76	0.59	0.37	0.01	0.03	1.57	2.42	0.97	4.02

^aEven though it is optically isotropic at visible wavelengths and has an amorphous micro-Raman pattern, preshock oscillatory zoning is preserved.

5.2. Formation Mechanisms and Conditions

Three specific models of solid-state formation of pressure-induced diaplectic glasses of silicate composition have been proposed (1) reversion of high-pressure phases to glass [Ahrens *et al.*, 1969], (2) metamict-like disordering of the structure at the unit cell scale by short-range atomic displacements [Ashworth and Schneider, 1985], and (3) pressure-induced formation of high-coordination glasses [Bunch *et al.*, 1967; Hemley *et al.*, 1988]. Our results are consistent with any of these models. Even though we do not currently see Si or a significant fraction of Al with high coordination in these samples, the static compression experiments of Williams and Jeanloz [1988] indicate that these high coordination Si and Al revert back to fourfold coordination upon decompression, and thus would not be expected to be remaining in our samples.

While our data does not allow us to definitively favor any model, the metamict-like disordering model [Ashworth and Schneider, 1985] is particularly attractive as it provides both conditions under which the deformation occurs and provides a specific mechanism by which the deformation occurs. In their model for the quartz-to-diaplectic silica transformation, the shock wave deforms the crystal lattice in a similar way as alpha particles do when they induce atomic displacements due to elastic collisions [Tomašić *et al.*, 2008]. Perhaps, an analogous process is occurring during the plagioclase to diaplectic plagioclase composition glass transformation. Furthermore, annealing of metamict silicates leads to recrystallization and recovery of original structure [Tomašić *et al.*, 2008; Beirau, 2012], a property that also occurs in shocked diaplectic plagioclase composition glasses [Bunch *et al.*, 1967; Ostertag, 1983].

It has been well established that shock effects in plagioclase are progressive [Stöffler, 1971; White, 1993; Fritz *et al.*, 2005; Jaret *et al.*, 2014]. As demonstrated previously [Kitamura *et al.*, 1977; White, 1993; Pickersgill, 2014], multiple types of maskelynite occur, such as the PDF-type glass confined to planar crystallographically controlled orientations, whole grain maskelynite with preserved texture, and an intermingling of these two types. The Lonar maskelynite studied here exhibits only whole grain-type maskelynite. Based on petrography, this sample is a Class 2 basalt [Kieffer *et al.*, 1976] with estimated shock pressures of ~25–~28 GPa. Although the maskelynite is fully optically isotropic at visible wavelengths, the pyroxenes remain birefringent (Figure 1), suggesting that the overall shock level was moderate in this sample. It is highly likely that the preservation of anisotropy within maskelynite occurs at moderate shock pressures just above the plagioclase-maskelynite transition. Therefore, our conclusions are only valid for maskelynite of moderate-level shock classes. For maskelynite of the moderate-level shock classes, we favor solid-state mechanisms for its formation but other mechanisms such as the shear band model [Grady, 1977] may be applicable to other varieties of shocked feldspar such as higher shocked samples from Lonar or the PDF-type maskelynite of White [1993].

6. Conclusions

We show that maskelynite formed at moderate shock level is the product of solid-state transformation and did not form through melting or quenching. Although maskelynite is isotropic at visible wavelengths and has Raman spectra identical to fused glass, X-ray total scattering data show a higher degree of intermediate range order and anisotropy in maskelynite. Additionally, infrared spectroscopy and X-ray total scattering experiments show differences due to orientation. Similarly, preservation of stoichiometric zoning within the maskelynite suggests minimal, if any, effect of heat during transformation to maskelynite. We favor a maskelynite formation mechanism that is purely solid state, such as the mechanical disaggregation of the crystal lattice [Hörz and Quaide, 1973; Arndt *et al.*, 1982] most likely by metamict-like destruction at the unit cell scale [Ashworth and Schneider, 1985].

This study also presents the first spectroscopic technique to distinguish shock-produced glass from thermally produced glass, which not only has implications for the formation mechanism of maskelynite but also for planetary remote sensing. For planetary remote sensing, our work may shed light onto the problem of distinguishing shock glasses from other amorphous materials, particularly on Mars. Recently, X-ray diffraction experiments on board the Mars Curiosity Rover have found abundant amorphous material, and there is considerable debate as to whether this material represents volcanic glass, highly weathered silica coatings, or shocked material from impact craters [Bish *et al.*, 2013]. Since we cannot distinguish shock-produced solid-state glass from fused glass via unoriented methods such as powder X-ray diffraction, like that on board Curiosity, shock processes cannot be ruled out as an explanation for amorphous material detected remotely on Mars. However, these techniques may be useful for distinguishing between shock-produced solid-state glass and fused glass in either Martian meteorites or samples that are cached and eventually returned to Earth.

Acknowledgments

S.J.J. is supported by a NASA Earth and Space Science Fellowship and the RIS⁴E team of the Solar System Exploration Research Virtual Institute (PI T. Glotch). This is SSERVI publication SERVII-2014-245. All data in this paper will be archived and made available on the Stony Brook University Vibrational Spectroscopy Laboratory's website: <http://aram.ess.sunysb.edu/tglotch>. We thank Don H. Lindsley (SBU) for assistance with fused glass synthesis and support for this through NASA MFR grant NNX13AG82G to H.N. We also thank Christopher Vidito (Rutgers) for assistance with the electron microprobe. Use of the National Synchrotron Light Source, Brookhaven National Laboratory, was supported by the U.S. Department of Energy, Office of Science, Office of Basic Energy Sciences, under contract DE-AC02-98CH10886. The X-ray total scattering experiments were supported by the U.S. Department of Energy (DOE) office of Basic Energy Sciences grant BES DE-FG02-09ER46650. The operation of the beamline X17B3 is partially supported by COMPRES, the Consortium for Materials Properties Research in Earth Sciences under NSF Cooperative agreement EAR 11-57758. This research used resources of the Advanced Photon Source, a U.S. Department of Energy (DOE) Office of Science User Facility operated for the DOE Office of Science by Argonne National Laboratory under contract DE-AC02-06CH11357. S.P.W. was supported by NASA PG&G award NNX14AP52G. This manuscript was greatly improved through conversations and discussion with Jessica Arnold, Christian Koeberl, and Jeffery Johnson.

References

- Ahrens, T. J., C. F. Petersen, and J. T. Rosenberg (1969), Shock compression of feldspars, *J. Geophys. Res.*, *74*, 2727–2746, doi:10.1029/JB074i010p02727.
- Alexopoulos, J. S., R. A. F. Grieve, and P. B. Robertson (1988), Microscopic lamellar deformation features in quartz: Discriminative characteristics of shock-generated varieties, *Geology*, *16*, 796–799, doi:10.1130/0091-7613(1988)016<0796:MLDFIQ>2.3.CO;2.
- Angeli, F., J. M. Delage, T. Charpentier, J. C. Petit, D. Ghaleb, and P. Faucon (2000), Influence of glass chemical composition on the Na-O bond distance: A ²³Na 3Q-MAS NMR and molecular dynamics study, *J. Non-Cryst. Solids*, *276*, 132–144, doi:10.1016/S0022-3093(00)00259-3.
- Arndt, J., W. Hummel, and I. Gonzalez-Cabeza (1982), Diaplectic labradorite glass from the Manicouagan Impact Crater: I. Physical properties, crystallization, structural, and genetic implications, *Phys. Chem. Mineral.*, *8*, 230–239, doi:10.1007/BF00309482.
- Ashworth, R., and H. Schneider (1985), Deformation and transformation in experimentally shock-loaded quartz, *Phys. Chem. Mineral.*, *11*, 241–249, doi:10.1007/BF00307401.
- Beirau, T. (2012), Annealing induced recrystallization of radiation damaged titanite and allanite, dissertation, Department of Earth Sciences, Univ. of Hamburg, Hamburg, Germany.
- Bischoff, A., and D. Stöffler (1984), Chemical and structural changes induced by thermal annealing of shocked feldspar inclusions in impact melt rocks from Lappjärvi, Finland, *J. Geophys. Res.*, *89*, B645–B656, doi:10.1029/JB089iS02p0645.
- Bish, D. L., et al. (2013), X-ray diffraction results from Mars Science Laboratory: Mineralogy of Rocknest at Gale Crater, *Science*, *341*, doi:10.1126/science.1238932.
- Boslough, M. B., R. T. Cygan, and G. A. Izett (1995), NMR spectroscopy of shocked quartz 706 from the K/T boundary: Shock-induced peak broadening, dense glass, and coesite, *Proc. Lunar Planet. Sci. Conf.* *26*, 149–150.
- Bunch, T. E., A. J. Cohen, and M. R. Dence (1967), Natural terrestrial maskelynite, *Am. Mineral.*, *52*, 244–253.
- Chao, E. C. T. (1968), Pressure and temperature histories of impact metamorphosed rocks—Based on petrographic observations, in *Shock Metamorphism of Natural Materials*, edited by B. M. French and N. M. Short, pp. 135–158, Mono Book Corp, Baltimore, Md.
- Chen, M., and A. El Goresy (2000), The nature of maskelynite in shocked meteorites: Not diaplectic glass but a glass quenched from shock-induced dense melt at high pressures, *Earth Planet. Sci. Lett.*, *179*, 489–502, doi:10.1016/S0012-821X(00)00130-8.
- Chupas, P. J., X. Qiu, J. C. Hanson, P. L. Lee, C. P. Grey, and S. J. L. Billinge (2003), Rapid-acquisition pair distribution function (RA-PDF) analysis, *J. Appl. Cryst.*, *36*, 1342–1347, doi:10.1107/S0021889803017564.
- Coster, D., A. L. Blumenfeld, and J. J. Fripiat (1994), Lewis acid sites and surface aluminum in aluminas and zeolites: A high-resolution NMR study, *J. Phys. Chem.*, *98*, 6201–6211, doi:10.1021/j100075a024.
- Cygan, R. T., M. B. Boslough, and B. J. Kirkpatrick (1992), NMR spectroscopy of experimentally shocked quartz and feldspar powders, in *Proceedings of the 22nd Lunar Planetary Science Conference*, pp. 127–136, Lunar and Planetary Institute, Houston, Tex.
- d’Espinoise de Lacaillerie, J. B., C. Fretigny, and D. Massiot (2008), MAS NMR spectra of quadrupolar nuclei in disordered solids: The Czjzek model, *J. Magn. Reson. Ser.*, *192*, 244–251, doi:10.1016/j.jmr.2008.03.001.
- Diemann, E., and J. Arndt (1984), Diaplectic glass from the impact Manicouagan crater II: X-ray studies and structural model, *Phys. Chem. Mineral.*, *11*, 178–181, doi:10.1007/BF00387849.
- El Goresy, A., B. Wopenka, M. Chen, and G. Kurat (1997), The Saga of maskelynite in Shergotty, 60th Annual Meteoritical Society Meeting, Abstract, 5037.
- El Goresy, A., P. Gillet, M. Miyahara, E. Ohtani, S. Ozawa, P. Beck, and G. Montagnac (2013), Shock-induced deformation of Shergottites: Shock-pressures and perturbations of magmatic ages on Mars, *Geochim. Cosmochim. Acta*, *101*, 233–262, doi:10.1016/j.gca.2012.10.002.
- Ferrière, L., and G. R. Osinski (2013), Shock metamorphism, in *Impact Cratering: Processes and Products*, edited by G. R. Osinski and E. Pierazzo, 316 pp., Wiley-Blackwell, Oxford.
- Fiske, P. S., W. J. Nellis, Z. Xu, and J. F. Stebbins (1998), Shocked quartz: A ²⁹Si magic-angle-spinning nuclear magnetic resonance study, *Am. Mineral.*, *83*, 1285–1292.
- Fredriksson, K., P. Brenner, A. Dube, D. Minton, C. Mooring, and J. Nelen (1979), Petrology, mineralogy, and distribution of Lonar (India) and lunar impact breccias and glasses, in *Smithsonian Contributions to the Earth Sciences: Mineral Sciences Investigations, 1976–1977*, vol. 22, pp. 1–13, Smithsonian Inst., Washington, D. C.
- Freeman, J. J., A. Wang, K. E. Kuebler, B. L. Jolliff, and L. A. Haskin (2008), Characterization of natural feldspars by Raman spectroscopy for future planetary exploration, *Can. Mineral.*, *46*, 1477–1500, doi:10.3749/canmin.46.6.1477.
- French, B. M., and C. Koeberl (2010), The convincing identification of terrestrial meteorite impact structures: What works, what doesn't, and why, *Earth Sci. Rev.*, *98*, 123–170, doi:10.1016/j.earscirev.2009.10.009.
- French, B. M., and N. M. Short (Eds.) (1968), *Shock Metamorphism of Natural Materials: Baltimore*, Mono Book Corporation, Md.
- Fritz, J., A. Greshake, and D. Stöffler (2005), Micro-Raman spectroscopy of plagioclase and maskelynite in Martian meteorites: Evidence of progressive shock metamorphism, *Antarct. Meteorite Res.*, *18*, 96–116.
- Grady, D. E. (1977), Processes occurring in shock-wave compression of rocks and minerals, in *High-Pressure Research: Applications to Geophysics*, edited by M. H. Anghnani and S. Akimoto, pp. 389–438, Academic Press, New York.
- Grady, D. E. (1980), Shock deformation of brittle solids, *J. Geophys. Res.*, *85*, 913–924, doi:10.1029/JB085iB02p00913.
- Hammersley, A. P., S. O. Svensson, M. Hanfland, A. N. Fitch, and D. Hausermann (1996), Two-dimensional detector software: From real detector to idealized image or two-theta scan, *High Pressure Res.*, *14*, 235–248, doi:10.1080/08957959608201408.
- Hanss, R. E., B. R. Montague, M. K. Davis, C. Galindo, and F. Hörz (1978), Pressure distribution in naturally and experimentally shocked granodiorites, *Proc. Lunar Planet. Sci. Conf. 9th*, pp. 2773–2787, Pergamon Press, Inc, New York.
- Hemley, R. J., A. P. Jephcoat, H. K. Mao, L. C. Ming, and M. H. Manghnani (1988), Pressure-induced amorphization of crystalline silica, *Nature*, *334*, 52–54, doi:10.1038/334052a0.
- Heymann, D., and F. Hörz (1990), Raman spectroscopy and X-ray diffractometer studies of experimentally produced diaplectic feldspar glass, *Phys. Chem. Mineral.*, *17*, 38–44, doi:10.1007/BF00209224.
- Hörz, F., and W. Quaide (1973), Debye-Scherrer investigations of experimentally shocked silicates, *The Moon*, *6*, 45–82, doi:10.1007/BF02630652.
- liishi, K., T. Tomisaka, T. Kato, and Y. Umegaki (1971), Isomorphous substitution and infrared and far infrared spectra of the feldspar group, *Neues Jahrb. Mineral. Abh.*, *115*, 98–119.
- Jaret, S. J., L. C. Kah, and R. S. Harris (2014), Progressive deformation of feldspar recording low barometry impact processes, Tenoumer impact structure, Mauritania, *Meteorit. Planet. Sci.*, *49*, 1007–1022, doi:10.1111/maps.12310.
- Johnson, J. R. (2012), Thermal infrared spectra of experimentally shocked andesine anorthosite, *Icarus*, *221*, 359–364, doi:10.1016/j.icarus.2012.08.012.
- Johnson, J. R., F. Hörz, P. G. Lucey, and P. R. Christensen (2002), Thermal infrared spectroscopy of experimentally shocked anorthosite and pyroxenites: Implications for remote sensing of Mars, *J. Geophys. Res.*, *107*(E10), 5073, doi:10.1029/2001JE001517.

- Johnson, J. R., F. Hörz, and M. I. Staid (2003), Thermal infrared spectroscopy and modeling of experimentally shocked plagioclase feldspars, *Am. Mineral.*, *88*, 1575–1582.
- Kieffer, S. W., R. B. Schaal, R. Gibbons, F. Hörz, D. J. Milton, and A. Dube (1976), Shocked basalt from Lunar impact crater, India, and experimental analogues, *Proc. Lunar Sci. Conf.*, *1*, 1391–1412.
- Kirkpatrick, R. J., R. A. Kinsey, K. A. Smith, D. M. Henderson, and E. Oldfield (1985), High resolution solid-state sodium-23, aluminum-27, and silicon-29 nuclear magnetic resonance spectroscopic reconnaissance of alkali and plagioclase feldspars, *Am. Mineral.*, *70*, 106–123.
- Kitamura, M., T. Goto, and Y. Syono (1977), Intergrowth textures of diaplectic glass and crystal in shock-loaded P-anorthosite, *Contrib. Mineral. Petrol.*, *61*, 299–304, doi:10.1007/BF00376703.
- Langenhorst, F. (2002), Shock metamorphism of some minerals: Basic introduction and microstructural observations, *Bull. Czech Geol. Surv.*, *77*, 265–282.
- Lee, S. K., S. Y. Park, H. I. Kim, O. Tschauner, P. Asimow, L. Bai, Y. Xiao, and P. Chow (2012), Structure of shock compressed model basaltic glass: Insights from O K-edge X-ray Raman scattering and high resolution ²⁷Al NMR spectroscopy, *J. Geophys. Res.*, *39*, L05306, doi:10.1029/2012GL050861.
- Mauri, F., A. Pasquarello, B. G. Pfommer, Y. G. Yoon, and S. G. Louie (2000), Si-O-Si bond-angle distribution in vitreous silica from first-principles ²⁹Si NMR analysis, *Phys. Rev. B: Condens. Matter*, *62*, R4786–R4789, doi:10.1103/PhysRevB.62.R4786.
- Melosh, H. J. (1989), *Impact Cratering: A Geologic Process*, 253 pp., Oxford Univ. Press, New York.
- Mernagh, T. P. (1991), Use of the laser Raman microprobe for discrimination amongst feldspar minerals, *J. Raman Spectrosc.*, *22*, 453–457, doi:10.1002/jrs.1250220806.
- Milton, D. J., and P. S. De Carli (1963), Maskelynite: Formation by explosive shock, *Science*, *140*, 670–671, doi:10.1126/science.140.3567.670.
- Osinski, G. R., and E. Pierazzo (2013), *Impact Cratering: Processes and Products*, 316 pp., Wiley-Blackwell, Oxford, U. K.
- Ostertag, R. (1983), Shock experiments on feldspar crystals, *J. Geophys. Res.*, *88*, B364–B376, doi:10.1029/JB088iS01p0B364.
- Pickersgill, A. E. (2014), Shock metamorphic effects in lunar and terrestrial plagioclase feldspar investigated by optical petrography and micro-X-ray diffraction, MS thesis, Univ. of Western Ontario – Electronic Thesis and Dissertation Repository. Paper 2094.
- Qiu, X., J. W. Thompson, and S. J. L. Billinge (2004), PDFgetX2: A GUI-driven program to obtain the pair distribution function from X-ray powder diffraction data, *J. Appl. Crystallogr.*, *37*, 678, doi:10.1107/S0021889804011744.
- Reeder, R. J., and F. M. Michel (2013), Application of total X-ray scattering methods and pair distribution function analysis for study of structure of biominerals, *Methods Enzymol.*, *532*, 477–500, doi:10.1016/B978-0-12-416617-2.00020-5.
- Reimold, W. U. (1982), The Lappajärvi meteorite crater, Finland: Petrography, Rb-Sr, major and trace element geochemistry of the impact melt and basement rocks, *Geochim. Cosmochim. Acta*, *46*, 1203–1225, doi:10.1016/0016-7037(82)90006-0.
- Rucks, M. J., J. A. Arnold, and T. D. Glotch (2015), Mid IR optical constants of triclinic minerals: A case study with labradorite, *Lunar Planet. Sci. Conf. 46th*, Abstract 2092.
- Sharma, S. K., B. Simons, and H. S. Yoder Jr. (1983), Raman study of anorthite, calcium Tschermak's pyroxene, and gehlenite in crystalline and glassy states, *Am. Mineral.*, *68*, 1113–1125.
- Short, N. M. (1969), Shock Metamorphism of Basalt, *Mod. Geol.*, *1*, 81–95.
- Singleton, A. C., G. R. Osinski, P. J. A. McCausland, and D. E. Moser (2011), Shock-induced changes in density and porosity in shock-metamorphosed crystalline rocks, Haughton impact structure, Canada, *Meteorit. Planet. Sci.*, *46*, 1774–1786, doi:10.1111/j.1945-5100.2011.01290.x.
- Son, T. H., and C. Koeberl (2007), Chemical variation in Lunar impact glasses and impactites, *GFF*, *129*(2), 161–176, doi:10.1080/11035890701292161.
- Stebbins, J. F., and X. Xue (2014), NMR spectroscopy of inorganic Earth materials, *Rev. Mineral. Geochem.*, *78*, 605–653, doi:10.2138/rmg.2014.78.15.
- Stöffler, D. (1971), Progressive metamorphism and classification of shocked and brecciated crystalline rocks at impact craters, *J. Geophys. Res.*, *76*, 5541–5551, doi:10.1029/JB076i023p05541.
- Stöffler, D. (1972), Deformation and transformation of rock-forming minerals by natural and experimental shock processes: I. Behavior of minerals under shock compression, *Fortschr. Mineral.*, *49*, 50–113.
- Stöffler, D., and U. Hornemann (1972), Quartz and feldspar glasses produced by natural and experimental shock, *Meteoritics*, *7*, 371–394, doi:10.1111/j.1945-5100.1972.tb00449.x.
- Stöffler, D., K. Keil, and E. R. D. Scott (1991), Shock metamorphism of ordinary chondrites, *Geochim. Cosmochim. Acta*, *55*, 3845–3867, doi:10.1016/0016-7037(91)90078-J.
- Thompson, L. (2012), Distribution and shock pressure formation for shatter cones: Insights from the Manicouagan impact structure, Canada (abstract), *Geol. Soc. Am. Abstr. Programs*, *44*, 629.
- Tomašić, N., V. Bermanec, A. Gajović, and M. R. Linarić (2008), Metamict Minerals: An insight into a relic crystal structure using XRD, Raman spectroscopy, SAED and HRTEM, *Croat. Chem. Acta*, *81*(2), 391–400.
- Treiman, A., and P. Treado (1998), Martian maskelynite? Raman spectra of plagioclase-composition glasses from ALH84001, EETA 79001, and ALHA 77005, *Lunar Planet. Sci. Conf. 29th*, Abstract 1196.
- Tschermak, G. (1872), Die Meteoriten von Schergotty und Gopalpur, *Sitzber. Akad. Wiss. Wien. Math. Naturwiss. Kl. Abt. I*, *65*, 122–146.
- Velde, B., and H. Boyer (1985), Raman microprobe spectra of naturally shocked microcline feldspars, *J. Geophys. Res.*, *90*, 3675–3682, doi:10.1029/JB090iB05p03675.
- von Engelhardt, W., and D. Stöffler (1968), Stages of shock metamorphism in crystalline rocks of the Ries basin, Germany, in *Shock Metamorphism of Natural Materials*, edited by B. M. French and N. M. Short, pp. 159–168, Mono Book Corp, Baltimore, Md.
- Wenk, H. R., W. Joswig, T. Tagai, M. Korekawa, and B. K. Smith (1980), Average structure of AN62-66 labradorite, *Am. Mineral.*, *65*, 81–85.
- White, J. C. (1993), Shock induced textures in plagioclase, Manicouagan, Quebec Canada, *Contrib. Mineral. Petrol.*, *113*, 524–532, doi:10.1007/BF00698320.
- Williams, Q., and R. Jeanloz (1988), Spectroscopic evidence for pressure-induced coordination changes in silicate glasses and melts, *Science*, *239*, 902–905.
- Wright, S. P. (2014), Lunar Crater, India: Analog for Mars in the field and in the laboratory, Abstract 1450 presented at Eighth International Conference on Mars.
- Wright, S. P., and H. E. Newsom (2013), Lunar Crater, India: An analog for Mars in the field and in the laboratory, Analog Sites for Mars Missions II, Abstract 4032.
- Wright, S. P., P. R. Christensen, and T. G. Sharp (2011), Laboratory thermal emission spectroscopy of shocked basalt from Lunar Crater, and implications for Mars orbital and sample data, *J. Geophys. Res.*, *116*, E09006, doi:10.1029/2010JE003785.
- Yang, W.-H., R. J. Kirkpatrick, N. Vergo, J. McHone, T. I. Emilsson, and E. Oldfield (1986), Detection of high pressure silica polymorphs in whole-rock samples from a meteor crater, Arizona, impact sample, using solid-state silicon-29 Nuclear Magnetic Resonance Spectroscopy, *Meteoritics*, *21*, 117–121.